

Emission Properties of a Hybrid Metallized Diamond(001) Photocathode

L. A. Angeloni, I-J. Shan, and W. Andreas Schroeder*

Department of Physics, University of Illinois Chicago, Chicago, IL 60607-7059, USA

ABSTRACT. The spectral emission characteristics of a proof-of-concept hybrid metallized diamond(001) photocathode are presented. The quantum efficiency (QE) is shown to be determined by the photo-injection efficiency across the ohmic contact at the back metallized face, whereas the mean transverse energy (MTE) of the photoemitted electrons is consistent with the a (optical)phonon-assisted and momentum-resonant Franck-Condon mechanism [*Phys. Rev. Applied* **23**, 054065 (2025)] following electron drift transport to the untreated diamond(001) front emission face. Emission is observed from both the lower and upper conduction bands of diamond with positive and negative electron affinity respectively. A potential route to the realization of a red-visible photocathode based on this concept with a sub-50meV MTE and a QE greater than 0.1% is discussed.

I. INTRODUCTION.

High-brightness and chemically robust solid-state laser-pulse-driven photocathodes that emit electrons at visible wavelengths are highly sought after as front-end electron sources [1-4] for x-ray free-electron lasers (XFELs) [5,6], ultrafast electron diffraction (UED) systems [7-11], and single-shot transmission electron microscopes [12-14]. Several semiconductor materials have been investigated for (and employed in) these applications; for example, Cs₂Te [15-18], Cs₃Sb [19-23], the bi-alkali antimonides [24-28], and Cesium semiconductors [29-35]. Most (if not all) of these high-brightness photocathodes are not sufficiently chemically robust to survive in air [1,2,36,37] and so require a (ultra)high vacuum environment for reliable operation and vacuum suitcases for transport. In contrast, robust ultra-wide bandgap semiconductors like diamond [38,39] and Gallium oxide [40] have not generally been considered for such applications, primarily due to their large intrinsic ~6eV work functions (valence band maximum to vacuum level). Fortunately, recent successful developments in Ohmic metal contacts for wide bandgap semiconductors [41-44] together with *n*-type doping provides an opportunity for a hybrid photocathode design in which the alignment of the Fermi level across the back metal-semiconductor interface allows for photo-injection of electrons from the metal into the conduction band (CB) of the semiconductor photocathode at visible to near ultraviolet wavelengths ($\lambda \gtrsim 350\text{nm}$). The subsequent cooling and transport dynamics of the photo-injected electrons in the semiconductor's CB determine their temperature T_e at the photocathode's front emission face and hence, with the electron affinity χ of the surface, the photocathode's emission properties [45-47].

In this article, we characterize the spectral emission characteristics of a proof-of-concept hybrid metallized diamond photocathode that exploits the recent development of Ohmic metallic contacts for diamond [41] to produce, using *n*-type Nitrogen doping, a robust photocathode with a sub-3.5eV near ultraviolet (UV) photoemission threshold. Both the quantum efficiency (QE) and the mean transverse energy (MTE) of electron photoemission are measured as a function of the incident photon energy – the latter being defined as $MTE = (\Delta p_T)^2 / 2m_0$, where Δp_T is the two-dimensional root-mean-square (rms) transverse momentum of the emitted electrons (i.e., parallel to the photocathode surface) and m_0 is the free electron mass. The MTE of the detected electron emission from the planar diamond(001) crystal face is shown to be dominated by a phonon-mediated Franck-Condon (FC) mechanism [47] due to the strong optical deformation potential scattering in diamond [39,48]. Emission from both the lower and upper conduction bands of diamond are observed. We also discuss approaches to improve the performance of hybrid metallized diamond photocathodes including the possibility of obtaining a red-visible photocathode with a sub-50meV MTE and a QE greater than 0.1%.

II. EXPERIMENT AND ANALYSIS DETAILS

The studied metallized single-crystal diamond(001) photocathode was fabricated by USA Applied Diamond Inc. [49]. The 5×5mm faced cuboid of 500μm length along the (001) emission direction was homoepitaxially grown via microwave assisted chemical vapor deposition (CVD). A further 10μm of 10ppm nitrogen doped material was grown on one of the faces (the “back” face) of each sample to reliably pin the Fermi level at the upper nitrogen state ~2.4eV below the conduction band minimum (CBM) [38,50,51] (Figure 1). On this doped face, 100nm of titanium, 100nm of platinum, and 1000nm of gold were sequentially deposited, resulting in the formation

*Contact author: andreas@uic.edu

of a titanium-carbide interface layer (an ‘ohmic’ contact) between the polycrystalline metals and the diamond [41]. The opposite face (the emission or “front” face) was polished to an optical quality with less than 2nm Ra, so that surface roughness effects [52,53] are not expected to influence the spectral characterization experiments to any significant extent.

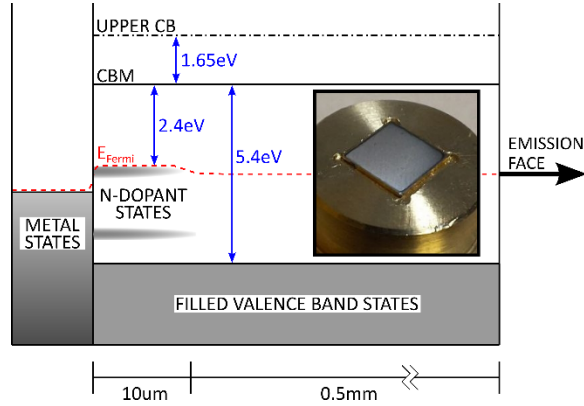


FIG 1. Energy-space schematic of the hybrid metallized diamond(001) photocathode. A 10 μ m Nitrogen-doped diamond layer pins the Fermi level (E_{Fermi}) at the 2.4eV activation energy of the upper Nitrogen dopant state, pulling the Ti metal states’ Fermi level to its energetic vicinity. Photo-injection of electrons from the metal states into the upper and lower conduction bands (separated by 1.65eV) provide the source for emission from the photocathode face after transport across its 0.5mm thickness. The inset shows the mounted 5 \times 5mm, 0.5mm-thick metallized diamond(001) photocathode.

The experimental QE and MTE data was obtained using the sub-picosecond tunable UV laser and the 10-20kV DC gun-based, 300K, photocathode characterization system described in Refs. 54 and 55. Briefly, a 20W, 16.7MHz femtosecond Yb: fiber laser system drives the optical parametric amplification of a nonlinear fiber generated continuum which is upconverted by sum frequency generation to produce \sim 0.5ps UV pulses. The resultant 10-100 μ W, p -polarized, 230-400nm radiation is focused at a 60° angle of incidence to an area of 2×10^{-4} cm 2 (\sim 120 \times 240 μ m elliptical spot size) on the photocathode surface producing an incident pulse intensity of less than 100kW/cm 2 – an irradiance that is much too small for significant two-photon absorption in diamond [56]. We also note that our entire 3.1-5.3eV UV tuning range is below the 5.4eV indirect bandgap of diamond [57,58], implying that all photoemitted electrons originate from the polycrystalline Ti metal deposited on the back photocathode face. After photo-injection

across the Ti-diamond interface, the electrons are transported in the diamond conduction band(s) to the hybrid photocathode’s front emission face (Figure 1) as a result of the internal field in the diamond generated by the applied \sim 1MV/m DC gun field. After acceleration in the DC gun, the photoemitted electrons enter a 42cm drift region before detection using a micro-channel plate (MCP)/phosphor screen detector (Beam Imaging Solutions; BOS 18) the output of which is imaged with 5:8 demagnification onto a 2.5 μ m pixel CMOS digital camera (Axiom Optics; FL-20BW), producing a \sim 20 μ m optical response point spread function corresponding to a \sim 1meV MTE resolution. The photocathode characterization system is calibrated for MTE measurements using accurate electron trajectory simulations and for QE measurements using the calibrated photocurrent detected by a Faraday cup from a Rh(110) photocathode [54].

Prior to the photocathode characterization measurements, the undoped front surface is irradiated for typically 20-30 minutes at \sim 1W/cm 2 by the 257nm ($\hbar\omega = 4.81$ eV) fourth harmonic of the Yb: fiber laser system. This *in-situ* ‘laser cleaning’ step in the \sim 10 $^{-8}$ torr vacuum chamber removes any organic contaminants from an initial optical cleaning of the photocathode with propanol and is performed with the electron gun under a normal 12-16kV operating bias. The laser cleaning process is terminated after \sim 20 minutes once the photocurrent (i.e., QE) stabilizes. It is possible that this sub-bandgap ‘hard’ UV-C laser irradiation also modifies the electronic properties of the back metal-diamond interface by, for example, redistributing the interface charge states by photoexcitation and recombination, but we expect this to be a minor effect for an ohmic contact.

Figure 2 displays a typical transverse electron beam profile measured by the CMOS digital camera for the hybrid metallized diamond(001) photocathode, in this case obtained at $\hbar\omega = 4.45$ eV. A thin transverse section through the center of this spatially resolved photo-electron signal can be readily decomposed (i.e., mathematically fit) into two Gaussian beams of different widths and amplitudes (right panel in Figure 2). The uncertainty in this analytical decomposition increases as the widths of the two Gaussians (i.e., the MTEs of the two photo-electron emission sources) become more equal to each and their amplitudes (i.e., relative QEs) diverge from each other. Nonetheless, the clean separation of the two signals in this manner allows their spectral emission characteristics to be studied independently. As discussed below, the spectral QE and MTE characteristics of these two beams are consistent with the emission of electrons

populating the upper and lower conduction bands of diamond [38].

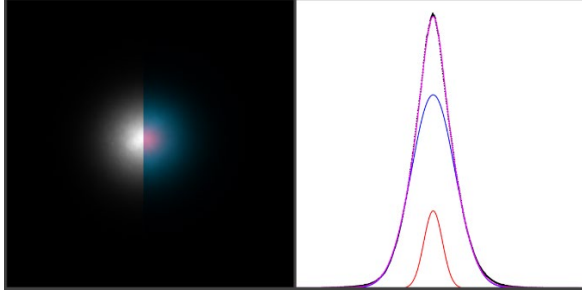


FIG 2. Two-component Gaussian signal decomposition. Left panel: Raw background subtracted digital signal at $\hbar\omega = 4.45\text{eV}$ (left half) and false color image of the two signal components (right half). Right panel: Fitted Gaussian spatial beam profiles to a horizontal section through the peak of the digital data (black dots). The sum of the weaker inner (red) and stronger outer (blue) Gaussians generate the fit (pink). The $\sim 3:1$ ratio of the outer to inner beam widths immediately give a $\sim 10:1$ MTE ratio as the horizontal (pixel) axis is directly related to the transverse momentum. Together with the $\sim 3:1$ peak height difference, this leads to $\sim 30:1$ ratio in the outer to inner signal strengths; that is, the smaller inner signal is $\sim 3\%$ of the total signal.

III. EXPERIMENTAL RESULTS AND DISCUSSION

Figure 3 displays the measured spectral dependences of the MTE from both the inner (lower MTE) and outer (higher MTE) beam signals from the 0.5mm-thick metallized diamond(001) photocathode. Immediately evident, after an emission threshold of $\sim 3.2\text{eV}$, is that (i) the MTE of both signals is constant as a function of the incident photon energy (i.e., independent of $\hbar\omega$) and (ii) the outer signal MTE is $\sim 10\times$ greater than the inner. These two observations are consistent with the ‘long transport’ regime for semiconductor photocathodes and the emission of electrons via a phonon-mediated, momentum-resonant, Franck-Condon process [39,47]. While the former is dictated by the physics of electron scattering processes [59] in the 0.5mm-thick diamond photocathode, the latter has already been shown to be the dominant emission mechanism for semiconductor photocathodes with a strong optical deformation potential [47] – optical phonon scattering allowing for emitted electrons to be both energy and momentum resonant with the recipient vacuum states. As shown in the Appendix, for a thermalized non-degenerate electron distribution,

the MTE (and QE) resulting from this type of emission mechanism is primarily dependent upon the electron affinity χ of the emitting band state and the temperature of the electron distribution T_e . For the case of a strong scattering interaction between electrons and optical phonons (i.e., a large dimensionless Fröhlich coupling constant g), as is the case for diamond [48], the optical phonon energy $\hbar\Omega$ also influences the photoemission characteristics as multi-phonon scattering becomes more probable during electron emission into the vacuum [39].

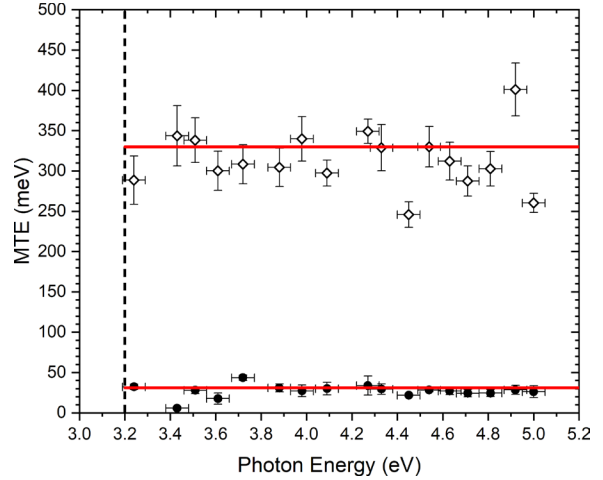


FIG 3. The measured MTE as a function of the incident photon energy for the inner (filled circles) and outer (open squares) signals. The horizontal red lines represent fits to the data using the momentum-resonant photon-mediated FC emission mechanism (see text). The vertical dashed line corresponds to the observed internal photo-injection threshold of $\phi_{\text{int}} = 3.2\text{eV}$.

A key to understanding the spectral emission properties of this hybrid diamond photocathode is therefore the determination of the temperature T_e of the electron distribution that drifts towards the (001) crystal emission face under the influence of the applied gun field. After photo-injection from the Ti metal into the diamond conduction band at the metallized back face, the electrons are expected to rapidly cool and generate a thermalized distribution at near the 300K lattice temperature by optical phonon scattering driven by the strong optical deformation potential of diamond [48] irrespective of their initial photo-excitation energy within the conduction bands. Thereafter, the 16kV/cm gun field forces them to drift towards photocathode emission face as the DC dielectric constant of 5.3 for diamond [60] implies an internal field of about 3kV/cm. For CVD grown undoped diamond, electron mobilities of around

*Contact author: andreas@uic.edu

4,000cm²/(V.s) have been measured at 300K [61] which for the internal applied gun field gives a drift velocity v_d of $\sim 1.2 \times 10^7$ cm/s; that is, about $0.6v_{ds}$ where the saturation drift velocity $v_{ds} \approx 2 \times 10^7$ cm/s [61] is associated with a saturation field strength of ~ 5 kV/cm. Analysis of equilibrium electron drift transport under polar optical scattering [59] for $v_d/v_{ds} \approx 0.6$ when $k_B T/\hbar\Omega = 6.6$, where T is the 300K lattice temperature and optical phonon energy $\hbar\Omega = 165$ meV [39,62], gives T_e/T of about 1.2; in other words, $k_B T_e \approx 30$ meV.

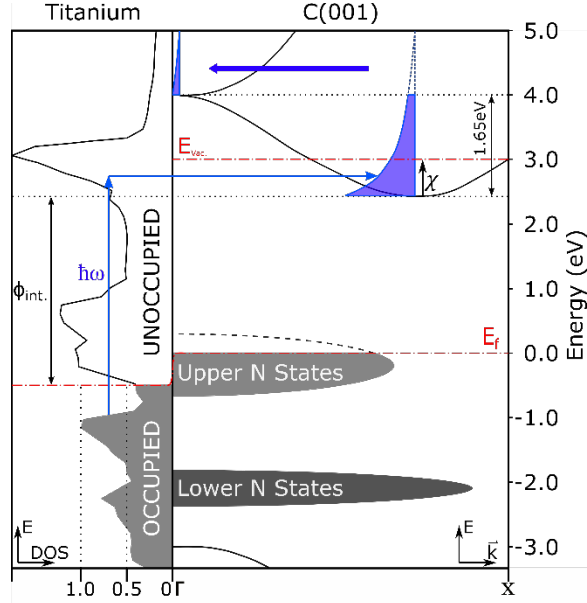


FIG 4. Density of states for polycrystalline Ti metal (left) and the Γ -X band structure of diamond with the upper and lower Nitrogen dopant states within the first 10 μ m of the metal-diamond interface (right). Electron photo-injected across the $\phi_{int.}$ potential barrier from the occupied metal states into the diamond conduction band generate a non-degenerate thermalized distribution (blue) the high energy portion of which populates the upper conduction band. For a bare, untreated diamond(001) surface, the vacuum energy level ($E_{vac.}$) resides between the lower and upper conduction band minima (as shown) and gives a positive value for the electron affinity χ .

Using this expected value for the average drift transport energy of the thermalized electron distribution and the analysis presented in the Appendix for phonon-assisted FC electron emission we obtain the upper and lower horizontal lines in Figure 3 using a fit to the MTE constrained by the known material and band structure properties of diamond [58]. First and foremost, it is known that the upper and lower conduction bands of diamond are separated in energy by 1.65eV [57,58,63] as shown in Figure 4 and that for

*Contact author: andreas@uic.edu

a bare (untreated) diamond(001) face the vacuum level is located between the upper and lower conduction band minima [38,64,65]. This means that the LCB has a positive electron affinity χ_{LCB} whereas the UCB has a negative electron affinity χ_{UCB} with a corresponding higher intrinsic QE: And one obtains the energy constraint $\chi_{LCB} - \chi_{UCB} = 1.65$ eV. Second, the strong optical deformation scattering in diamond leads to a renormalization of the electron energy in the bands due to the formation of polarons [66]. For an intrinsic dimensionless Fröhlich coupling constant g_0 and a band electron effective mass m^* , the renormalization energy is given by $\sqrt{m^*/m_0} g_0 \hbar\Omega$ [66,67] – the real part of the electron self-energy shift above the (conduction) band minimum associated with the polaron quasi-particle [39,68]. Consequently, for the electron population in a band, the effective electron affinity $\chi^* = \chi + \sqrt{m^*/m_0} g_0 \hbar\Omega$. Combined, these two physical properties give the modified energy constraint

$$\chi_{LCB} - \chi_{UCB} = 1.65\text{eV} + g_0 \hbar\Omega \left(\sqrt{\frac{m_{UCB}^*}{m_0}} - \sqrt{\frac{m_{LCB}^*}{m_0}} \right).$$

Thus, since $g_0 \approx 1.0$ for diamond [39], with $m_{UCB}^* = 0.42m_0$ [38] and $m_{LCB}^* = 1.2m_0$ in the (001) propagation (and emission) direction [58], we obtain $\chi_{LCB}^* - \chi_{UCB}^* \approx 1.58$ eV for the energetic difference between the electron populations in the upper and lower CBs at $k_B T_e \approx 30$ meV. Further, as the effective Fröhlich coupling constant $g = \sqrt{m^*/m_0} g_0$ is different for the upper and lower conduction bands, the Poisson statistics governing multi-phonon FC emission from the two bands will be different. Specifically, the strength of the n^{th} phonon FC emission process is given by $e^{-g} g^n/n!$ [39,69], where $n = 0, 1, 2, 3, \dots$, implying that an appropriately weighted (and terminated) sum is required to evaluate the total QE and hence also the MTE of electron emission as described in the Appendix (equations A6 and A7).

The two horizontal lines in Figure 3 use the known physical parameters of diamond (g_0 , $\hbar\Omega$, m_{UCB}^* , and m_{LCB}^*), $k_B T_e = 30$ meV, and values of $\chi_{LCB} = 0.81(\pm 0.05)$ eV and $\chi_{UCB} = -0.84(\pm 0.05)$ eV in fitting the experimental MTE data to Appendix equations A6 and A7 for NEA and PEA FC emission from the upper and lower conduction bands respectively. The uncertainties quoted for the two electron affinities are reflective of the rms fit to the experimental data. Inclusion of uncertainties in the two-signal extraction etc. yield an overall uncertainty of around ± 0.1 eV, giving $\chi_{LCB} \approx 0.6$ to 0.8 eV which is consistent with literature values for a bare (untreated) diamond(001)

surface [64,65]. As this PEA for the LCB is much greater than $k_B T_e$, only electrons in the high energy (exponential) tail of the band's thermalized electron distribution above the vacuum level can emit. As shown by equation A6 for the FC emission mechanism under PEA conditions, this produces an MTE $\approx k_B T_e$, supporting the suggestion that the measured inner MTE signal is due to LCB emission. The negative value for χ_{UCB} is then also consistent with the observation of a larger 330meV MTE for the outer signal originating from UCB FC emission as the leading term in equation A7 is proportional to $\frac{1}{2}|\chi_{UCB}| = 0.42(\pm 0.05)\text{eV}$ with multi-phonon emissions ensuring a somewhat lower overall MTE due to energy-momentum restrictions in the available vacuum states (see Appendix) [39,47].

In contrast to the MTE, the spectral dependence of the total QE (the sum of LCB and UCB emissions) is not dependent on the dynamics of the drift electron transport in the hybrid diamond photocathode as for any incident photon energy the electron temperature T_e at the photocathode emission face is constant at about 360K – the parameter that dictates the QE for the FC emission mechanism for the fixed material constants g_0 , χ , and $\hbar\Omega$ (see Appendix). Consequently, the QE should be solely determined by the injection efficiency across the back ohmic metal-diamond interface as recombination effects during drift transport are insignificant in the high-quality CVD-grown undoped diamond due to filled valence band states. Shown in Figure 5 is the measured spectral dependence of the photocathode's QE together with a fit of the form $QE = A_1(\hbar\omega - \phi_1)^{3/2} + A_2(\hbar\omega - \phi_2)^{3/2}$, where $\phi_1 = 3.2\text{eV}$ (the emission threshold energy associated with the Fermi level in the Ti metal (see Figure 4)) and $\phi_2 = 3.7\text{eV}$ which corresponds to the threshold energy required to promote electrons into the LCB from the second step in the occupied density of states (DOS) in the polycrystalline Ti metal evident in Figure 4. The fit therefore assumes a stepwise constant DOS in the Ti metal (the electron source), and a uniform transmission (for each DOS step) over the internal potential barrier into the recipient LCB states described using a standard DOS for a parabolic band of the form $\sqrt{E}dE$ for the energy interval E to $E+dE$ integration over which gives the $E^{3/2}$ dependence for the total number of injected electrons. However, the ratio $A_1:A_2$ of 1:15 obtained from the fit is significantly greater than the 1:2 ratio in the DOS step (Figure 4). We attribute this difference to the fact that our *ab initio* band structure calculations indicate that the Ti states contributing to the second step in the DOS are generally at momenta that are a better match to the states around the minimum of the LCB, resulting in an

*Contact author: andreas@uic.edu

increased injection efficiency. The reasonable fit to the experimental data is therefore direct evidence that the QE is only dependent upon the injection efficiency across its back metal-diamond interface, and thus that this hybrid photocathode operates in the long transport regime with T_e just above the lattice temperature [47].

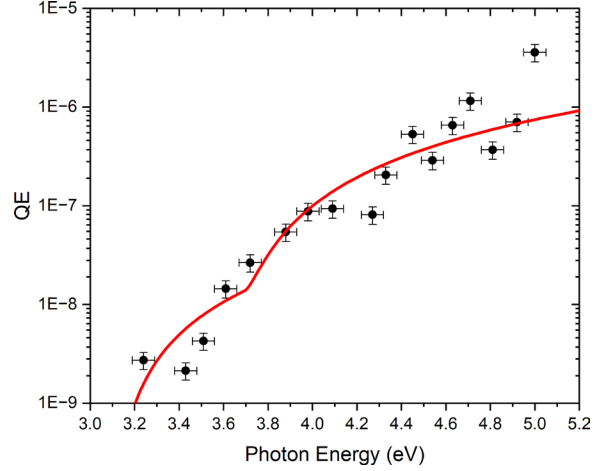


FIG 5. The measured QE as a function of the incident photon energy for the hybrid photocathode. The solid line is a fit to the data of the form $QE = A_1(\hbar\omega - \phi_1)^{3/2} + A_2(\hbar\omega - \phi_2)^{3/2}$, with $\phi_1 = \phi_{\text{int.}} = 3.2\text{eV}$ and $\phi_2 = 3.7\text{eV}$, associated with a two-step increase in the polycrystalline Ti density of states (see Figure 4), and $A_1 = 4 \times 10^{-8}\text{eV}^{-3/2}$ and $A_2 = 6 \times 10^{-7}\text{eV}^{-3/2}$.

As the two signals from the upper and lower conduction bands were separated in our analysis, the spectral dependence of the ratio of the UCB to LCB emission quantum efficiencies can also be determined. Within experimental uncertainty of a few percent associated with the two-signal decomposition, the QE of the inner LCB signal is found to be relatively constant at $\sim 5\%$ of the total signal over the entire investigated spectral range. This is consistent with expectations when one considers the expected theoretical QE ratio for the two bands, their relative population densities, and the diamond band structure (Figure 4). For $k_B T_e = 30\text{meV}$ and in the limit of zero phonon energy ($\hbar\Omega \rightarrow 0$), the FC emission mechanism predicts a minimum expected intrinsic QE ratio that is given approximately by $\exp[\chi_{LCB}/(k_B T_e)] : 1$ favoring the UCB [47] (see Appendix). On the other hand, the thermalized population density ratio between the lower and upper conduction bands is about $\exp[(\chi_{LCB} - \chi_{UCB})/(k_B T_e)] : 1$ respectively, giving a net $\exp[-\chi_{UCB}/(k_B T_e)] \sim 10^{11}$ favoring LCB emission in the employed parabolic band

approximation. However, as seen in Figure 4, the LCB dispersion along ΓX falls away from parabolic for energies more than $\sim 0.5\text{eV}$ above its minimum, and indeed its DOS goes to zero at the Γ point 1.65eV above the LCB minimum [58]. In-house *ab initio* band structure calculations further indicate that the LCB also falls away from a parabolic energy-momentum dependence in the directions transverse to ΓX . In addition, the LCB is cut-off by the Brillouin zone edge at the X point around 0.5eV above its minimum (Figure 4). Together, the resulting substantial reduction in the available DOS in the six LCBs above the vacuum level will force a significant redistribution of carriers to maintain an overall thermalized 360K electron distribution pushing many more electrons into the singular UCB and thus offset the $\exp[-\chi_U/(k_B T_e)] \sim 10^{11}$ factor favoring LCB emission. Moreover, the strong optical deformation potential scattering in diamond will allow the population in the NEA UCB to be continually replenished even in the face of its much larger intrinsic QE [47], thereby further offsetting the expected stronger emission from the LCB. The experimental data indicates that these physical effects suppress the LCB FC emission by a factor of $\sim 10^{12}$ so that the UCB emission becomes $\sim 20\times$ stronger than that of the LCB.

We also note that both the experimental MTE and QE data clearly indicate that the internal photo-injection threshold $\phi_{\text{int.}} = \phi_1 \approx 3.1\text{eV}$ is around 0.7eV greater than the 2.4eV threshold expected when the Fermi level is pinned by the upper nitrogen dopant level [38,50,51] and energetically level with that in the Ti metal. The likely explanation is the formation of a Ti-C bond dipole at the interface produced by the metallization, plus some downward band bending towards the interface in the doped n -type region [42]. The metal-diamond interface is therefore not completely ohmic as it has a directional character akin to a p - n junction, i.e. a Schottky barrier.

IV. FUTURE DIRECTIONS

Further optimization of the performance of metallized diamond(001) photocathodes is possible at both the emission face and the back photo-injection interface. For the latter, n -type doping with phosphorous rather than nitrogen at the back metallized surface is expected to reduce the photo-injection threshold to less than 1.5eV even with the 0.7eV Ti-C back-surface dipole since the donor activation energy of phosphorous is around 0.57eV [70] giving $\phi_{\text{int.}} \approx 1.3\text{eV}$ with the same Fermi level pinning. This would then produce a ‘red’ photocathode (photoemission at wavelengths greater than 600nm) with similar spectral properties to those of the N-doped variant

*Contact author: andreas@uic.edu

characterized above with photon energies shifted down by $1.5\text{-}2\text{eV}$.

The QE of this type of hybrid photocathode can also be dramatically increased by using surface terminations to reduce the work function of the emission face and hence the electron affinity of the LCB where the vast majority of the photoinjected carriers reside in the long transport regime with $k_B T_e \approx 30\text{meV}$. For example, H-termination of a diamond(001) surface has been shown to produce $\chi_{\text{LCB}} \approx -0.5\text{eV}$ [39,71] which would theoretically be expected to increase the front face emission efficiency by a factor of $\exp[\chi/(k_B T_e)] \approx 10^7$ [47], implying that overall QE of the resulting photocathode will likely be solely limited by the back-face photo-injection efficiency. However, this is also expected to produce an MTE of around 280meV (see equation A3 or A7). An emitted electron beam with a smaller MTE of $40\text{-}50\text{meV}$ should be generated for near zero electron affinity for the LCB with perhaps only a factor of 10 reduction in the QE (see equation A4 or A5). Provided a suitable robust surface termination can be found to facilitate $\chi_{\text{LCB}} \approx 0$ for diamond(001) using a P-doped back face metallization, this could produce a useful ‘high brightness’ visible (red) photocathode.

In addition, the work of Chang et al. [72] indicates that metallized diamond(001) photocathode could generate an effective QE well above unity through avalanche amplification of the electron emission under high gun fields – an effect that exploits the inherent robustness of diamond. This would, however, likely substantially increase the electron temperature T_e at the photocathode front face and thus the MTE of electron emission. One would also need to be careful in their use in RF guns since the gun frequency ν_{RF} will need to be significantly less than $\nu_{\text{ds}}/z_{\text{cath.}}$ – the reciprocal of the electron transit time over the photocathode length $z_{\text{cath.}}$. For the above case, $z_{\text{cath.}} = 0.5\text{mm}$ and using the saturation drift velocity $\nu_{\text{ds}} \approx 2 \times 10^7 \text{cm/s}$ for diamond [61] one obtains $\nu_{\text{RF}} \ll 400\text{MHz}$; for example, placing the 185.7MHz LCLS-II RF gun [73] too close to the limit unless $z_{\text{cath.}}$ is reduced to less than $100\mu\text{m}$. However, the smaller photocathode crystal length will also reduce any net avalanche amplification by more than a factor of 100 from $z_{\text{cath.}} = 0.5\text{mm}$.

We note that there is also a limit to how small $z_{\text{cath.}}$ can be if one wishes to maintain a spectrally independent $k_B T_e \approx 30\text{meV}$ (and hence an MTE $< 50\text{meV}$ when $\chi \approx 0$) for diamond in the long transport limit [47]. Specifically, this requires that steady-state drift transport be established. As the characteristic optical photon emission time for an electron in the CB of diamond is $\sim 5\text{fs}$ [74], electrons photo-injected into the

CB with an excess energy of 1eV could cool to within $\hbar\Omega = 165\text{meV}$ [39,62] of the band minimum in around 30fs, but are more likely to initially cool to $k_B T_e \approx 200\text{meV}$ – the equipartition electron energy with the two (TO and LO) optical phonon modes [47] – with further cooling delayed by the $\sim 7\text{ps}$ optical phonon decay time [62]. The latter longer time then gives the requirement that $z_{\text{cath.}}$ be greater than $\sim 1\mu\text{m}$, again using $v_{\text{ds}} \approx 2 \times 10^7 \text{cm/s}$ as the limiting electron velocity [61]. As this photocathode thickness is less than the $10\mu\text{m}$ doped region used to pin the Fermi level (Figure 1), which could perhaps be halved, a reasonable practical limit for a sub-50meV MTE hybrid metallized diamond(001) photocathode at 300K is that $z_{\text{cath.}} > 10\mu\text{m}$. This would give a minimal electron transit (i.e., transport) time over $z_{\text{cath.}}$ of 50-100ps and thus allow the operation of a visible (red) photocathode in a sub-GHz RF gun.

Metallized ‘dielectric’ photocathodes that employ robust wide band gap semiconductors other than diamond can also be envisioned. For example, ohmic metal contacts on *n*-type (Si-doped) Gallium nitride (GaN) [75] and (Sn-doped) Gallium oxide (Ga_2O_3) [76] could potentially allow for efficient photo-injection over a sub-0.5eV back surface potential barrier. The strong optical deformation potential scattering with $\hbar\Omega \approx 90\text{meV}$ in both materials [77,78] would then be expected to produce $k_B T_e$ less than 50meV for drift transport at 300K [59] and thus a low MTE for electron emission with $\chi \approx 0$ through the described phonon-mediated FC mechanism. Further and in contrast to diamond, the lowest CB in both GaN and Ga_2O_3 is located at the Γ point of the Brillouin zone [76,79] which means that direct emission [80] from the CB will be significantly more efficient due to intrinsic near band-to-vacuum momentum matching at $\chi \approx 0$. As these CBs have an electron effective mass m^* of around $0.2m_0$ [76,81], an $MTE \approx \left(\frac{m^*}{m_0}\right) k_B T_e$ of less than 10meV may be expected from direct band emission.

There have also been several prior studies of hybrid dielectric on metal photocathodes where $z_{\text{cath.}}$ is significantly less than 100nm [82-88]. In particular, the deposition of a 3nm layer of CsI on Cu(001) resulted in a three orders of magnitude QE enhancement at 266nm [84]. From the viewpoint of this article, these hybrid photocathodes are clearly in the short transport regime (if electrons occupy the dielectric CB states) where equipartition of the electron energy with optical phonon modes and band bending effects are important [47]. The alternative emission mechanism is that the photoemitted electrons are ‘transported’ through the CB of the thin dielectric

layer without appreciable scattering as has been demonstrated for a $\sim 2\text{nm}$ -thick Cs_2Te layer on GaAs [89]. In either case, the MTE of emission at 300K is likely to be large ($>100\text{meV}$) [86] unless (i) the emitting electron distribution has a low temperature ($T_e \rightarrow 300\text{K}$) from near threshold photo-injection from the metal [88], and/or (ii) $\chi \geq 0$ if three-dimensional (i.e., near bulk-like) optical phonon scattering effects are prevalent for the confined vibrational lattice modes of the thin dielectric film.

IV. SUMMARY COMMENTS

The spectral emission properties of a hybrid metallized diamond(001) photocathode are presented and shown to be consistent with a phonon-mediated FC process – a momentum-resonant emission mechanism that is expected to be dominant for semiconductor photocathodes with sufficiently strong optical deformation potential scattering [47]. Two emission signals are observed, both displaying an MTE independent of the incident photon energy; (i) a weak inner signal with a low MTE of around 30meV and (ii) a stronger outer signal with an MTE of 330meV. These two signals can be well described by the FC emission theory (see Appendix) with the appropriate material parameters and the physics associated with drift transport to the diamond(001) emission face. Specifically, a standard semiconductor transport analysis under the applied $\sim 3\text{kV/cm}$ internal field [59] indicates that after rapid initial cooling by optical phonon emission the resultant thermalized electron distribution photo-injected from the metallized back face drifts with $k_B T_e \approx 30\text{meV}$ over the 0.5mm photocathode thickness; that is, in the ‘long’ transport regime [47]. This allows the weaker inner signal to be identified as being due to FC emission from the lower conduction band with a PEA of $\chi_{\text{LCB}} \approx 0.8\text{eV}$, since for FC dominated emission the MTE tends to $k_B T_e$ for χ much greater than $k_B T_e$ [47] (Appendix equation A1). The larger 330meV MTE of the stronger outer signal may then be rationally associated with FC emission from the upper conduction band with a NEA of $\chi_{\text{UCB}} \approx -0.85\text{eV}$. This interpretation of the experimental MTE data is further supported by the spectral dependence of the QE which is observed to be consistent with the expected photo-injection efficiency across the back polycrystalline Ti to diamond interface – all the emitted electrons being generated at the hybrid photocathode’s back metallized face as the incident photon energies are less than the 5.4eV diamond bandgap, and the constant electron temperature T_e of 360K at all incident photon energies (due to the long transport regime) implying a constant intrinsic QE for emission from both the upper and lower conduction bands.

*Contact author: andreas@uic.edu

We note that the agreement between the experimental MTE data and the phonon-mediated FC emission process using just four parameters (T_e , χ , $\hbar\Omega$, and the Fröhlich coupling constant g_0) is obtained without considering the energy bandwidth of the optical phonons involved in the momentum-resonant scattering of electrons into the vacuum states. In general, one would expect this bandwidth to be convolved with the electron energy distribution in its ‘mapping’ onto the vacuum states [47], causing the energy width of the emitted electrons to increase as n (the number of phonons involved) increases. Such an effect is expected to be observable when $\hbar\Omega$ is significantly greater than $k_B T_e$ and indeed has been for a hydrogen-terminated diamond(001) photocathode [39]. Its effect on the MTE is however not expected to be significant since the Poisson statistics dictate that the strength of the n^{th} FC emission process is proportional to $e^{-g} g^n / n!$ [39,69] and so declines rapidly as n increases for $n > g$ – noting that g_0 is of the order unity for diamond [39].

It is also to be noted that the results presented here are in apparent contradiction to those of a heavily N-doped photocathode [38] where it was shown that the electron temperature T_e at emission was dependent on the incident photon energy $\hbar\omega$, generating non-monotonic variations in the emitted MTE (and QE) as the average initial electron temperature changed due to different dominant photoexcitation mechanisms. We believe that this fundamental difference in the emission characteristics of the two photocathodes is related to the large difference in their photoexcited electron population densities. For the heavily N-doped case, photoexcitation into the CB states by linear absorption occurs over a 400 μm -thick doped region. On the other hand, for the hybrid photocathode, the photo-injected ‘sheet’ charge is expected to have a thickness much less than 100nm – an upper limit of 100nm being inferred from the product of the $v_{\text{ds}} \approx 2 \times 10^7 \text{cm/s}$ saturation drift velocity [61] and the $\sim 0.5 \text{ps}$ laser pulse duration. For equivalent excitation probabilities into the CB(s) of diamond for our $\sim 10 \text{nJ/cm}^2$ UV incident laser pulse fluence, around 10^6 electrons are excited per pJ-level laser pulse, giving a photoexcited electron density of $\sim 10^{11} \text{cm}^{-3}$ for the N-doped photocathode and likely greater than $\sim 10^{15} \text{cm}^{-3}$ for the hybrid photocathode. The inter-electron (charge) separation is therefore more than $10\times$ greater for the N-doped case ($\sim 1 \mu\text{m}$) than the metallized diamond(001) photocathode (less than 100nm). Thus, the requirement that $2/g \approx 2$ electrons interact with one optical phonon for polaron-mediated electron transport [59] is much more probable for the hybrid photocathode; indeed,

*Contact author: andreas@uic.edu

“Frohlich” polarons associated with a long-range electron-phonon interaction have a radius very much greater than the crystal lattice parameter [90] resulting in coherent motion with a free carrier (electron) mobility $\mu_e \gg 1 \text{cm}^2/(\text{V}\cdot\text{s})$ – as is observed in diamond [61]. Conversely, therefore, the ‘single’ electron picture of transport and emission employed to describe the spectral properties of the N-doped diamond(001) photocathode [38] is a also valid approximation.

ACKNOWLEDGEMENTS

The authors are also indebted to the Physical Sciences Machine Shop for their assistance and expertise. This work was supported by the U.S. Department of Energy under Award no. DE-SC0020387.

DATA AVAILABILITY

The data that support the findings of this article are openly available [91].

APPENDIX

As outlined in Ref. 47, our theoretical analysis of electron emission by a momentum-resonant phonon-mediated FC mechanism involves the mapping of the electron distribution in the emitting semiconductor band states onto the vacuum states using the appropriate representation of the electron flux \mathbf{j} over the photoemission barrier; namely, $j \propto p_0 \cos\theta$, where p_0 is the electron momentum in the vacuum and θ is its angle with respect to the photocathode surface normal. The representation of the electron flux in this manner is forced by the momentum resonance which sets the wave function probability of transmission over the photoemission barrier to unity. Under the assumption of a non-degenerate thermalized electron distribution at temperature T_e in the photocathode band states, the direct mapping for $\hbar\Omega \rightarrow 0$ generates the following results [47]:

$$MTE = k_B T_e \left[\frac{3k_B T_e + \chi}{2k_B T_e + \chi} \right] \quad (\text{A1})$$

$$QE \propto (k_B T_e)^2 [2k_B T_e + \chi] \exp \left[-\frac{\chi}{k_B T_e} \right] \quad (\text{A2})$$

for positive electron affinity ($\chi > 0$), and

$$MTE = \frac{|\chi|}{2} + k_B T_e \left[\frac{3k_B T_e + |\chi|}{2k_B T_e + |\chi|} \right] \quad (\text{A3})$$

$$QE \propto (k_B T_e)^2 [2k_B T_e + |\chi|] \quad (\text{A4})$$

for negative electron affinity ($\chi < 0$), where k_B is Boltzmann's constant. These relations also assume a low QE (less than about 10%) such that the emission is a small perturbation on the electron distribution in the semiconductor band states (i.e. produces a negligible change in T_e).

For photocathode materials like diamond, which have a large phonon energy $\hbar\Omega$ and a large intrinsic Fröhlich coupling constant g_0 , equations A1-A4 describing the MTE and QE resulting from the FC emission process must be modified to account for energy shifts and multi-phonon emission. First, the real part of the electron self-energy shift associated with the polaron quasi-particle [39,66] produces an effective electron affinity $\chi + g\hbar\Omega$, where χ is the electron affinity associated with the actual band minimum (calculated by, for example, density functional theory (DFT)) and $g = g_0\sqrt{m^*/m_0}$ with m^* the effective electron mass of the band in the emission (transport) direction [47]. Second, the electrons in the thermalized polaron quasi-particle distribution can either be directly FC emitted ($n = 0$) or be emitted through (multi)-phonon emission ($n \geq 1$) [39] with the strength of the n^{th} FC emission process given by Poisson statistics as $e^{-g}g^n/n!$ [39,69]. For the case when k_BT_e is significantly less than $\hbar\Omega$, this generates a cascade of emission 'replicas' of the portions of the thermalized electron distribution that can emit (i.e., are above the vacuum level after losing $n\hbar\Omega$ of energy) – as observed by Rameau et al. [39]. In other words, in the above expressions for FC emission, $\chi \rightarrow \chi + (g - n)\hbar\Omega$ for $n = 0, 1, 2, 3 \dots$ with the n^{th} emission weighted by $e^{-g}g^n/n!$, and one needs to sum over n to determine the total electron emission so that, for example, equation A4 for the total QE for NEA is modified to read

$$QE \propto \sum_{n=0}^N \frac{e^g g^n}{n!} (k_B T_e)^2 [2k_B T_e + |\chi + (g - n)\hbar\Omega|] \quad (\text{A5})$$

where the upper limit N in the summation is determined by physical constraints (e.g., lack of vacuum states) or practical expediency associated with the rapid convergence of the series.

Applying this procedure to evaluate the total MTE is straightforward since, for independent emission processes, it is simply expressed as the sum of the individual MTEs of the n^{th} emission weighted by the QE of that emission all divided by the total QE. For the case of positive electron affinity, the result is

MTE

$$= k_B T_e \frac{\sum_{n=0}^{\infty} \frac{g^n}{n!} [3k_B T_e + \chi + (n - g)\hbar\Omega] \cdot \exp\left(-\frac{n\hbar\Omega}{k_B T_e}\right)}{\sum_{n=0}^{\infty} \frac{g^n}{n!} [2k_B T_e + \chi + (n - g)\hbar\Omega] \cdot \exp\left(-\frac{n\hbar\Omega}{k_B T_e}\right)} \quad (\text{A6})$$

which is technically only valid for $\chi > g\hbar\Omega$ to ensure that the effective electron affinity $\chi + (n - g)\hbar\Omega$ is positive for $n = 0$; that is, the effective conduction band minimum, including the real part of the electron self-energy shift associated with the polaron quasi-particle [39,68], is below the vacuum level. In practice, the summations need not be extended to infinity as the $g^n/n!$ factor from the Poisson statistics of phonon emission [39,69] ensures that both series quickly converge for sufficiently large n . In fact, for diamond, where $g \approx 1$ [39], even without the $\exp[-n\hbar\Omega/(k_B T_e)]$ factor, four phonon emission ($n = 4$) is only $\sim 4\%$ of the peak emission at $n = 1$ and accounts for less than 2% of the total emission. Consequently, termination of the two series at $n = 4$ introduces an uncertainty of significantly less than 1% in the theoretical evaluation of the MTE.

For the case of negative electron affinity, the result is

MTE

$$= \frac{\sum_{n=0}^N \frac{g^n}{n!} [|\chi + (n - g)\hbar\Omega|^2 + 4k_B T_e |\chi + (n - g)\hbar\Omega| + 6(k_B T_e)^2]}{2 \sum_{n=0}^N \frac{g^n}{n!} [2k_B T_e + |\chi + (n - g)\hbar\Omega|]} \quad (\text{A7})$$

which is valid for a negative effective electron affinity $\chi + (n - g)\hbar\Omega$; that is, for n less than $g + \chi/(\hbar\Omega)$ which gives the maximum integer N for the summations. For $n > g + \chi/(\hbar\Omega)$, the effective electron affinity for the FC emission process becomes positive and the emission efficiency is strongly reduced due to the $\exp[-n\hbar\Omega/(k_B T_e)]$ factor (equation A6). Consequently, for nearly all cases, the evaluation of the MTE up to $n = N$ is sufficient, even discounting the $g^n/n!$ factor from the Poisson statistics of phonon emission [39,69].

We also note only optical phonon emission is considered in the presented FC emission theory. For the case of a non-degenerate thermalized electron distribution in diamond presented in this article, where $k_B T_e \approx 30\text{meV}$ and $\hbar\Omega \approx 160\text{meV}$ [39,62], this is a very good approximation since the expected ratio of phonon emission to phonon absorption is greater than 100:1 [59]. Only when $k_B T_e$ is greater than $\hbar\Omega$ will this approximation start to break down.

REFERENCES

1. D.H. Dowell, I. Bazarov, B. Dunham, K. Harkey, C. Hernandez-Garcia, R. Legg, H. Padmore, T. Rao, J. Smedley, and W. Wan, "Cathode R&D for future light sources," Nucl. Instrum. Methods Phys. Res. A **622**, 685 (2010).
2. R. Xiang and J. Schaber, "Review of recent progress on advanced photocathodes for superconducting RF gun," Micromachines **13**, 1241 (2022).
3. P. Michelato, "Photocathodes for RF photoinjector," Nucl. Inst. & Meth. A **393**, 455 (1997).
4. P. Musumeci, J. Giner Navarro, J.B. Rosenzweig, L. Cultrera, I. Bazarov, J. Maxson, S. Karkare, and H. Padmore, "Advances in bright electron sources," Nucl. Inst. & Meth. A **907**, 209 (2018).
5. P. Emma, R. Akre, J. Arthur, R. Bionta, C. Bostedt, J. Bozek, A. Brachmann, P. Bucksbaum, R. Coffee, F. J. Decker, Y. Ding, D. Dowell, S. Edstrom, A. Fisher, J. Frisch, S. Gilevich, J. Hastings, G. Hays, Ph Hering, Z. Huang, R. Iverson, H. Loos, M. Messerschmidt, A. Miahnahri, S. Moeller, H. D. Nuhn, G. Pile, D. Ratner, J. Rzepiela, D. Schultz, T. Smith, P. Stefan, H. Tompkins, J. Turner, J. Welch, W. White, J. Wu, G. Yocky, J. Galayda, "First lasing and operation of an ångstrom-wavelength free electron laser," Nat. Photonics **4**, 641 (2010).
6. H.N. Chapman, A. Barty, M.J. Bogan, S. Boutet, M. Frank, S.P. Hau-Riege, S. Marchesini, B.W. Woods, S. Bajt, W.H. Benner, R.A. London, E. Plönjes, M. Kuhlmann, R. Treusch, S. Düsterer, T. Tschentscher, J.R. Schneider, E. Spiller, T. Möller, C. Bostedt, M. Hoener, D.A. Shapiro, K.O. Hodgson, D. van der Spoel, F. Burmeister, M. Bergh, C. Caleman, G. Huldt, M.M. Seibert, F.R.N.C. Maia, R.W. Lee, A. Szöke, N. Timneanu, and J. Hajdu, "Femtosecond diffractive imaging with a soft-x-ray free-electron laser," Nature Phys. **2**, 839 (2006).
7. G. Sciani and R. J. D. Miller, "Femtosecond electron diffraction: Heralding the era of atomically resolved dynamics," Rep. Prog. Phys. **74**, 096101 (2005).
8. J. Hastings, F. Rudakov, D. Dowell, J. Schmerge, J. Cardoza, J. Castro, S. Gierman, H. Loos, and P. M. Weber, "Ultrafast time-resolved electron diffraction with megavolt electron beams," Appl. Phys. Lett. **89**, 184109 (2006).
9. R. Li, C. Tang, Y. Du, W. Huang, Q. Du, J. Shi, L. Yan, and X. Wang, "Experimental demonstration of high quality MeV ultrafast electron diffraction," Rev. Sci. Instrum. **80**, 083303 (2009).
10. P. Musumeci, J. Moody, C. Scoby, M. Gutierrez, H. Bender, and N. Wilcox, "High quality single shot diffraction patterns using ultrashort megaelectron volt beams from a radio frequency photoinjector," Rev. Sci. Instrum. **81**, 013306 (2010).
11. S. Weathersby, G. Brown, M. Centurion, T.F. Chase, R. coffee, J. Corbett, J.P. Eichner, J.C. Frisch, A.R. Fry, M. Gühr, N. Hartmann, C. Hast, R. Hettel, R.K. Jobe, E.N. Jongewaard, J.R. Lewandowski, R.K. Li, A.M. Lindenberg, I. Makasyuk, J.E. May, D. McCormick, M.N. Nguyen, A.H. Reid, X. Shen, K. Sokolowski-Tinten, T. Vecchione, S.L. Vetter, J. Wu, J. Yang, H.A. Dürr, and X.J. Wang, "Mega-electron-volt ultrafast electron diffraction at SLAC National Accelerator Laboratory," Rev. Sci. Instrum. **86**, 073702 (2015).
12. T. LaGrange, M.R. Armstrong, K. Boyden, C.G. Brown, G.H. Campbell, J.D. Colvin, W.J. DeHope, A.M. Frank, D.J. Gibson, F.V. Hartemann, J.S. Kim, W.E. King, B.J. Pyke, B.W. Reed, M.D. Shirk, R.M. Shuttlesworth, B.C. Stuart, B.R. Torralva, and N.D. Browning, "Single-shot dynamic transmission electron microscopy," Appl. Phys. Lett. **89**, 044105 (2006).
13. Y. Murooka, N. Naruse, S. Sakakihara, M. Ishimaru, J. Yang, and K. Tanimura, "Transmission-electron diffraction by MeV electron pulses," Appl. Phys. Lett. **98**, 251903 (2011).
14. R. K. Li and P. Musumeci, "Single-shot MeV transmission electron microscopy with picosecond temporal resolution," Phys. Rev. Appl. **2**, 1-15 (2014).
15. S. Quan, J. Hao, L. Lin, F. Zhu, F. Wang, L. Feng, S. Huang, Z. Wang, X. Wen, P. Fan, H. Xie, K. Liu, K. Zhao, and J. Chen, "Stable operation of the DC-SRF photoinjector," Nucl. Instrum. Meth. A **798**, 117 (2015).
16. N. Terunuma, A. Murata, M. Fukuda, K. Hirano, Y. Kamiya, T. Kii, M. Kuriki, R. Kuroda, H. Ohgaki, K. Sakaue, M. Takano, T. Takatomi, J. Urakawa, M. Washio, Y. Yamazaki, and J. Yang, "Improvement of an S-band RF gun with a Cs₂Te photocathode for the KEK-ATF," Nucl. Inst. & Meth. A **613**, 1 (2010).

*Contact author: andreas@uic.edu

17. E. Prat, S. Bettoni, H.-H. Braun, R. Ganter, and T. Schietinger, "Measurements of copper and cesium telluride cathodes in a radio-frequency photoinjector," *Phys. Rev. STAB* **18**, 043401 (2015).
18. F. Zhou, C. Adolphsen, A. Benwell, G. Brown, D.H. Dowell, M. Dunning, S. Gilevich, K. Grouev, G. Huang, B. Jacobson, X.H. Liu, A. Miahnahri, F. Sannibale, J. Schmeger, and T. Vecchione, "Commissioning of the SLAC Linac Coherent Light Source II electron source," *Phys. Rev. Accel. & Beams* **24**, 073401 (2021).
19. W. Spicer, "Photoemissive, photoconductive, and optical absorption studies of alkali-antimony compounds," *Phys. Rev.* **112**, 114 (1958).
20. L. Cultrera, I. Bazarov, A. Bartnik, B. Dunham, S. Karkare, R. Merluzzi, and M. Nichols, "Thermal emittance and response time of a cesium antimonide photocathode," *Appl. Phys. Lett.* **99**, 152110 (2011).
21. L. Cultrera, S.Karkare, H. Lee, X. Liu, I. Bazarov, and B. Dunham, "Cold electron beams from cryocooled, alkali antimonide photocathodes," *Phys. Rev. STAB* **18**, 113401 (2015).
22. A. Galdi, J. Balajka, W. DeBenedetti, L. Cultrera, I. V. Bazarov, M. Hines, and J. M. Maxson, "Reduction of surface roughness emittance of Cs₃Sb photocathodes grown via codeposition on single crystal substrates," *Appl. Phys. Lett.* **118**, 244101 (2021).
23. C. T. Parzyck, A. Galdi, J.K. Nangoi, W.J.I. DeBenedetti, J. Balajka, B.D. Faeth, H. Paik, C. Hu, T.A.Arias, M.A. Hines, D.G. Schlom, K.M. Shen, and J.M. Maxson, "Single-crystal alkali antimonide photocathodes: High efficiency in the ultrathin limit," *Phys. Rev. Lett.* **128**, 114801 (2022).
24. D.H. Dowell, K.J. Davis, K.D. Friddell, E.L. Tyson, C.A. Lancaster, L. Milliman, R.E. Rodenburg, T. Aas, M. Bemes, S.Z. Bethel, P.E. Johnson, K. Murphy, C. Whelen, G.E. Busch, and D.K. Remelius, "First operation of a photocathode radio frequency gun injector at high duty factor," *Appl. Phys. Lett.* **63**, 2035 (1993).
25. T. Vecchione, I. Ben-Zvi, D.H. Dowell, J. Feng, T. Rao, J. Smedley, W. Wan, and H. Padmore, "A low emittance and high efficiency visible light photocathode for high brightness accelerator-based X-ray light sources," *Appl. Phys. Lett.* **99**, 034103 (2011).
26. E. Wang, V.N. Litvinenko, I. Pinayev, M. Gaowei, J. Skaritka, S. Belomestnykh, I. Ben-Zvi, J.C. Brutus, Y. Jing, J. Biswas, J. Ma, G. Narayan, I. Petrushina, O. Rahman, T. Xin, T. Rao, F. Severino, K. Shih, K. Smith, G. Wang, and Y. Wu, "Long lifetime of bialkali photocathodes operating in high gradient superconducting radio frequency gun," *Sci. Rep.* **11**, 4477 (2021).
27. I. Bazarov, L. Cultrera, A. Bartnik, B. Dunham, S. Karkare, Y. Li, X. Liu, J. Maxson, and W. Roussel, "Thermal emittance measurements of a cesium potassium antimonide photocathode," *Appl. Phys. Lett.* **98**, 224101 (2011).
28. J. Maxson, L. Cultrera, C. Gulliford, and I. Bazarov, "Measurement of the tradeoff between intrinsic emittance and quantum efficiency from a NaKSb photocathode near threshold," *Appl. Phys. Lett.* **106**, 234102 (2015).
29. W. Spicer, "Negative affinity 3-5 photocathodes: Their physics and technology," *Appl. Phys.* **12**, 115 (1977).
30. D. Pierce and F. Meier, "Photoemission of spin-polarized electrons from GaAs," *Phys. Rev. B* **13**, 5484 (1976).
31. J. Kirschner, H. P. Oepen, and H. Ibach, "Energy- and spin-analysis of polarized photoelectrons from NEA GaAs," *Appl. Phys. A* **30**, 177 (1983).
32. I. Bazarov, B. M. Dunham, Y. Li, X. Liu, D. Ouzounov, C. Sinclair, F. Hannon, and T. Miyajima, "Thermal emittance and response time measurements of negative electron affinity photocathodes," *J. Appl. Phys.* **103**, 054901 (2008).
33. S. Uchiyama, Y. Takagi, M. Niigaki, H. Kan, and H. Kondoh, "GaN-based photocathodes with extremely high quantum efficiency," *Appl. Phys. Lett.* **86**, 103511 (2005).
34. I. Bazarov, B. Dunham, X. Liu, M. Virgo, M. Dadiran, F. Hannon, and H. Sayed, "Thermal emittance and response time measurements of a GaN photocathode," *J. Appl. Phys.* **105**, 083715 (2009).
35. S. Levenson, M. Andorf, B. Dickensheets, I. Bazarov, A. Galdi, J. Encomendero, V. Protasenko, D. Jena, H. Xing, and J. M. Maxson, "Measurement of spin-polarized photoemission from wurtzite and zinc blende gallium nitride photocathodes," *Appl. Phys. Lett.* **125**, 034107 (2024).
36. N. Chanlek, J. Herbert, R. Jones, L. Jones, K. Middleman, and B.L. Militsyn, "The degradation of quantum efficiency in negative electron affinity

*Contact author: andreas@uic.edu

- GaAs photocathodes under gas pressure”, *Appl. Phys.* **47**, 055110 (2014).
37. L. Jones, H. Scheibler, S. Kosolobov, A. Terekhov, B. Militsyn, and T. Noakes, “Non-monotonic behaviour in the mean transverse energy of electrons emitted from a reflection-mode p-GaAs(Cs,O) photocathode during its QE degradation through oxygen exposure”, *J. Phys. D: Appl. Phys.* **54**, 205301 (2021).
 38. L. Angeloni, S. Baryshev, M. Mühle, and W. A. Schroeder, “Spectral Emission Properties of a Nitrogen-doped Diamond(001) Photocathode: Hot Electron Transport and Transverse Momentum Filtering,” *Phys. Rev. B* **107**, 165105 (2023).
 39. J. D. Rameau, J. Smedley, E. M. Muller, T. E. Kidd, and P. D. Johnson, “Properties of hydrogen terminated diamond as a photocathode,” *Phys. Rev. Lett.* **106**, 137602 (2011): This work gives an effective Fröhlich coupling constant $g = \sqrt{m^*/m_0} g_0 = 1.1(\pm 0.01)$ for the LCB of diamond with an effective mass of $m^* = 1.2m_0$ in the (001) emission direction, so that the intrinsic Fröhlich coupling constant $g_0 \approx 1.0$.
 40. L.A. Angeloni, I-J. Shan, J.H. Leach, and W.A. Schroeder, “Iron dopant energy levels in β -Ga₂O₃,” *Appl. Phys. Lett.* **124**, 252104 (2024).
 41. H. Hoff, G. Waytena, C. Vold, J. Suehle, I. Isaacson, M. Rebbert, D. Ma, and K. Harris, “Ohmic contacts to semiconducting diamond using Ti/Pt/Au trilayer metallization scheme”, *Diam. Rel. Meter.* **5**, 1450 (1996).
 42. Yuan Liu, “Recent research on ohmic contacts on GaN-based materials,” *IOP Conf. Ser.: Mater. Sci. Eng.* **738**, 012007 (2020).
 43. L.A.M. Lyle, “Critical review of Ohmic and Schottky contacts to β -Ga₂O₃”, *J. Vac. Sci. Technol. A* **40**, 060802 (2022).
 44. O. Sadowski, M. Kaminski, A. Taube, J. Tarenko, M. Guiziewicz, M. Wzorek, J. Maleszyk, I. Jozwik, A. Szerling, P. Prystawko, M. Bockowski, and I. Grzegory, “Low-resistivity Ti/Al/TiN/Au ohmic contacts to Ga- and N-face n-GaN for vertical power devices,” *Phys. Status Solidi A* **221**, 2400076 (2024).
 45. S. Karkare, D. Dimitrov, W. Schaff, L. Cultrera, A. Bartnik, X. Liu, E. Sawyer, T. Esposito, and I. Bazarov, “Monte Carlo charge transport and photoemission from negative electron affinity GaAs photocathodes,” *J. Appl. Phys.*, vol. 113, p. 104904, 2013; Erratum, *J. Appl. Phys.* **117**, 109901 (2015).
 46. J. Marini, L. Bell, and F. Shahedipour-Sandvik, “Monte Carlo simulation of III-nitride photocathodes,” *J. Appl. Phys.* **123**, 124502 (2018).
 47. W.A. Schroeder, L.A. Angeloni, I-J. Shan, and L.B. Jones, “Franck-Condon electron emission from polar semiconductor photocathodes,” *Phys. Rev. Applied* **23**, 054065 (2025). DOI: <https://doi.org/10.1103/PhysRevApplied.23.054065>
 48. W. Pötz and P. Vogl, “Theory of optical-phonon deformation potentials in tetrahedral semiconductors,” *Phys. Rev. B* **24**, 2025 (1981).
 49. USA Applied Diamond Inc.; <http://www.usapplieddiamond.com>
 50. E. Rohrer, C. F. O. Graeff, R. Janssen, C. E. Nebel, M. Stutzmann, H. Güttler, and R. Zachai, “Nitrogen-related dopant and defect states in CVD diamond,” *Phys. Rev. B* **54**, 7874 (1996).
 51. J. Rosa, M. Vaněček, M. Nesládek, and L. M. Stals, “Photoionization cross-section of dominant defects in CVD diamond,” *Diamond and Rel. Mat.* **8**, 721 (1999).
 52. S. Karkare and I. Bazarov, “Effects of surface nonuniformities on the mean transverse energy from photocathodes,” *Phys. Rev. Applied* **4**, 024015 (2015).
 53. Z. Zhang and C. Tang, “Analytical study on emittance growth caused by roughness of a metallic photocathode,” *Phys. Rev. ST Accel. Beams* **18**, 053401 (2015).
 54. G. Adhikari, P. Riley, and W.A. Schroeder, “Spectral characterization of a Rh(110) photocathode: Band structure interpretation,” *AIP Advances* **9**, 065305 (2019).
 55. L. Angeloni, I-J. Shan, and W. A. Schroeder, “Sub-threshold ultrafast one-photon photoemission from a Cu(111) photocathode,” *AIP Advances* **12**, 105129 (2022).
 56. J.I. Dadap, G.B. Focht, D.H. Reitze, and M.C. Downer, “Two-photon absorption in diamond and its application to ultraviolet femtosecond pulse-width measurement,” *Optics Letters* **16**, 499 (1991).
 57. D. C. Clark, P. J. Dean, and P. V. Harris, “Intrinsic absorption edge in diamond,” *Proc. R. Soc. Lond. A* **277**, 312-329 (1964).
 58. H. Löfås, A. Grigoriev, J. Isberg, and R. Ahuja, “Effective masses and electronic structure of diamond including electron correlation effects in

- first principles calculations using the *GW*-approximation,” AIP Advances **1**, 032139 (2011).
59. K. Seeger, "Semiconductor Physics – An Introduction," in Springer Series in Solid-State Sciences 40 (Springer Verlag, Berlin, 1989).
 60. L. G. Groves and A. E. Martin, "The dielectric constant of diamond," Trans. of Faraday Society **35**, 575 (1940).
 61. C.J.H. Wort and R.S. Balmer, "Diamond as an electronic material" Materials Today **11**, 22 (2008).
 62. K. Ishioka, M. Hase, and M. Kitajima, "Coherent optical phonons in diamond," Appl. Phys. Lett. **89** (2006) 231916.
 63. F. Giustino, S. G. Louie, and M. L. Cohen, "Electron-phonon renormalization of the direct band gap of diamond," Phys. Rev. Lett. **105**, 265501 (2010).
 64. L. Diederich, O. M. Küttel, P. Aebi, and L. Schlapbach, "Electron affinity and work function of differently oriented and doped diamond surfaces determined by photoelectron spectroscopy," Surf. Sci. **418**, 219 (1998).
 65. M.J. Rutter and J. Robertson, "*Ab initio* calculation of electron affinities of diamond surfaces," Phys. Rev. B **57**, 9241 (1998).
 66. J. T. Devreese, "Polarons," in Encyclopedia of Applied Physics, vol. 14, pp.383-409 (Wiley-VCH Publishers Inc., Weinheim, 1996).
 67. M. E. Mora-Ramos, F. J. Rodriguez and L. Quiroga, "Polarons in Wurtzite Nitride Semiconductors," Solid State Communications **109**, 767 (1999).
 68. G.D. Mahan, Many-Particle Physics 2nd ed., New York: Plenum Press, 1990.
 69. K. Ishizaka, R. Eguchi, S. Tsuda, A. Chainani, T. Yokoya, T. Kiss, T. Shimojima, T. Togashi, S. Watanabe, C.-T. Chen, Y. Takano, M. Nagao, I. Sakaguchi, T. Takenouchi, H. Kawarada, and S. Shin, "Temperature-dependent localized excitations of doped carriers in superconducting diamond," Phys. Rev. Lett. **100**, 166402 (2008).
 70. Y. Katamune, A. Izumi, K. Ichikawa, and S. Koizumi, "Heavy phosphorous doping of diamond by hot-filament chemical vapor deposition," Diamond and Rel. Mater. **134**, 109789 (2023).
 71. J. van der Weide, Z. Zhang, P. K. Baumann, M. G. Wensell, J. Bernholc, and R. J. Nemanich, "Negative-electron-affinity effects on the diamond (100) surface," Phys. Rev. B **50**, 5803 (1994).
 72. X. Chang, Q. Wu, I. Ben-Zvi, A. Burrill, J. Kewisch, T. Rao, J. Smedley, E. Wang, E.M. Muller, R. Busby, and D. Dimitrov, "Electron beam emission from a diamond-amplifier cathode," Phys. Rev. Lett. **105**, 164801 (2010).
 73. F. Zhou, C. Adolphsen, D. Dowell, and R. Xiang, "Overview of CW electron guns and LCLS-II RF gun performance," Front Phys. **11**, 1150809 (2023).
 74. N. Tandon, J. D. Albrecht, and L. R. Ram-Mohan, "Electron-phonon coupling and associated scattering rate in diamond," Diamond & Related Materials **56**, 1-5 (2015).
 75. W. Götz, N.M. Johnson, C. Chen, H. Liu, C. Kuo, and W. Imler, "Activation energies of Si donors in GaN," Appl. Phys. Lett. **68**, 3144 (1996).
 76. Jiaye Zhang, Jueli Shi, Dong-Chen Qi, Lang Chen, and K.H.L. Zhang, "Recent progress on the electronic structure, defect, and doping properties of Ga₂O₃" APL Mater. **8**, 020906 (2020).
 77. V.Yu. Davydov, Yu.E. Kitaev, I.N. Goncharuk, A.N. Smirnov, J. Graul, O. Semchnova, D. Uffmann, M.B. Smirnov, A.P. Mirgorodsky, and R.A. Evarestov, "Phonon dispersion and Raman scattering in hexagonal GaN and AlN," Phys. Rev. B **58**, 12899, (1998).
 78. B.M. Jensen, R. Gillen, Z. Galazka, J. Maultzsch, and M.R. Wagner, "First- and second-order Raman spectroscopy of monoclinic β -Ga₂O₃," Phys. Rev. Mater. **6**, 054601 (2022).
 79. I. Vurgaftman and J.R. Meyer, "Band parameters for nitrogen-containing semiconductors," J. Appl. Phys. **94**, 3675 (2003).
 80. W. Schroeder and G. Adhikari, "Evaluation of photocathode emission properties in an electron gun: One-step photoemission from bulk-band to vacuum states," New J. Phys. **21**, 033040 (2019).
 81. A. Udabe, I. Baraia-Etxaburu, and D. G. Diez, "Gallium Nitride Power Devices: A State of the Art Review," IEEE Access **11**, pp. 48627-48647 (2023).
 82. K. Németh, K.C. Harkay, M. van Veenendaal, L. Spentzouris, M. White, K. Attenkofer, and G. Srager, "High-brightness photocathodes through ultrathin surface layers on metals," Phys. Rev. Lett. **104**, 276801 (2001).
 83. W. He, S. Vilayurganapathy, A.G. Joly, T.C. Droubay, S.A. Chambers, J.R. Maldonado, and W.P. Hess, "Comparison of CsBr and KBr coated Cu photocathodes: Effects of laser irradiation and

- work function changes,” *Appl. Phys. Lett.* **102**, 071604 (2013).
84. L. Kong, A.G. Joly, T.C. Droubay, Y. Gong, and W.P. Hess, “Enhanced quantum efficiency from hybrid Cesium halide/copper photocathodes,” *Appl. Phys. Lett.* **104**, 171106 (2014).
 85. J. Droubay, L. Kong, S.A. Chambers, and W.P. Hess, “Work function reduction by BaO: Growth of crystalline barium oxide on Ag(001) and Ag(111) surfaces,” *Surface Sci.* **632**, 201 (2015).
 86. T.C. Droubay, S.A. Chambers, A.G. Joly, W.P. Hess, K. Németh, K.C. Harkay, and L. Spentzouris, “Metal-insulator photocathode heterojunction for directed electron emission,” *Phys. Rev. Lett.* **112**, 067601 (2014).
 87. L. Kong, A.G. Joly, T.C. Droubay, and W.P. Hess, “Quantum efficiency enhancement in CsI/metal photocathodes,” *Chem. Phys. Lett.* **621**, 155 (2015).
 88. C. Benjamin, H.M. Chum, T.J. Rehaag, L.A.J. Soomary, C.P. Welsch, L.B. Jones, T.C.Q. Noakes, and G.R. Bell, “Enhanced performance of an Ag(100) photocathode by an ultra-thin MgO film,” *J. Appl. Phys.* **132**, 195303 (2022).
 89. J. K. Bae, L. Cultrera, P. DiGiacomo, and I. Bazarov, “Rugged spin-polarized electron sources based on negative electron affinity GaAs photocathode with robust Cs₂Te coating,” *Appl. Phys. Lett.* **112**, 154101 (2018).
 90. C. Franchini, M. Reticioli, M. Setvin, and U. Diebold, “Polarons in materials,” *Nature Reviews Materials* **6**, 560 (2021).
 91. <https://figshare.com/s/4191828b961d7789c673>